An innovative accelerated stress test representative of automotive PEMFC degradation mechanisms validated on 1000 hours real-world operation

Elena Colombo[*1], *Andrea Baricci*[1], *Daniele Mora*[1], *Laure Guetaz*[2], *Andrea Casalegno*[1]

[1]Politecnico di Milano, Department of Energy, Via Lambruschini 4, 20156, Milano, Italy
[2]CEA, LITEN, Université Grenoble Alpes, 17 Rue des Martyrs, 38054, Grenoble, France

[*] Corresponding author: elena.colombo@polimi.it

Abstract

Automotive Polymer Electrolyte Membrane Fuel Cells (PEMFC) must improve their durability to increase competitiveness; quantifying the degradation at reduced costs and time is a relevant topic for developing the technology. For this reason, accelerated stress tests (ASTs) were standardized over the years aiming at accelerating the progress of durable materials. However, state-of-the-art ASTs are effective to selectively accelerate the degradation of each component, but are difficult to correlate to real-world ageing. To overcome this issue, this study presents a novel operational mode hydrogen/air AST, which mimics in a comprehensive and representative way the driving functioning (namely low power, high power and stops) by reproducing stressors that reflect operating conditions and mitigation strategies adopted in the application. The ageing results of three state-of-the-art PEMFC are successfully correlated to 1000 operating hours of realistic load cycling. Decays of cell voltage, mass transport resistance, electrocatalyst nanoparticles distribution and efficiency were correlated, identifying a 10-fold acceleration in testing time. Cathode catalyst active surface area is reduced to 61÷65% of the initial value and promoted transport losses were mainly related to the cathode thin-film resistance. Performance indicators mostly changed within the first 400 cycles, while predictions highlighted a progressive slowing down of rates of decay.

Keywords

Polymer Electrolyte Membrane Fuel Cell, automotive, durability, degradation, AST, efficiency loss.

1. List of Acronyms and Abbreviations

AST	Accelerated Stress Test
BoT	Beginning of Test
CCM	Catalyst Coated Membrane
CL	Catalyst layer
CV	Cyclic Voltammetry
$d_{v/a}$	Average volume/area diameter
DLC	Dynamic load cycle protocol
ECSA	Electrochemically active catalyst surface area
EIS	Electrochemical Impedance Spectroscopy
F	Faraday's constant
GDL	Gas Diffusion Layer
GSA	Geometric Surface Area
HFR	High Frequency Resistance
HP	High Power
i	Current density
LHV	Lower Heating Value
LP	Low Power
LSV	Linear Sweep Voltammetry
MEA	Membrane Electrode Assembly
Mm^{H2}	Hydrogen Molar Mass
MPL	Microporous layer
NP	Nanoparticle
OCV	Open Circuit Voltage
p	Pressure
PEMFC	Polymer Electrolyte Membrane Fuel Cell
PFSA	Perfluorosulfonic acid polymers
rf	Catalyst roughness factor
R	Molar gas constant
RH	Relative Humidity
R_{local}	Local thin-film transport resistance
$R_{MT,O2}$	Oxygen Mass Transport Resistance
R_{PI}	Pressure independent component of mass transport resistance
$R_{PI,gas}$	Pressure independent component of transport resistance due to Knudsen diffusion

$R_{PI,ion}$	Pressure independent component of mass transport resistance due to ionomer thin-film
SEM	Scanning Electron Microscopy
TEM	Transmission Electron Microscopy
x^{dry}_{O2}	oxygen dry mole fraction
ΔV	Cell voltage
η	Energy efficiency

2. Introduction

Polymer Electrolyte Membrane Fuel Cells (PEMFC) vehicles using hydrogen as a fuel are a crucial market for reducing the emissions of greenhouse gases. This technology is of great interest because of the efficient energy conversion but it still presents some weaknesses as the cost and the durability competitiveness [1]. To promote the fuel cell automotive vehicles commercialization, the European Commission set the 2030 lifetime goal [2] at 7'000 hours of operation. At the present stage, 5'000 hours of duration have been reached, but at an initial cost not yet competitive compared to the fossil fuel-based solutions. The approaches researched for the cost reduction can relevantly reduce the stack lifetime, affected by the PEMFC performance decay, which is driven by the degradation mechanisms that occur under the dynamic operations of real systems. In a previous work [3], 1'000 operating hours of a real-world complete degradation test were studied. The activity was realized under the ID-FAST H2020 European project, in the frame of which the load cycle protocol [4] was designed, starting from a vehicles fleet dataset. The combination of different measurement techniques provided a wide understanding of the underlaying ageing mechanisms.

The most relevant degradation mechanism usually highlighted in automotive-like conditions is the loss of the electrochemically active surface area of platinum catalyst (ECSA) at the cathode electrode, where it is present as carbon supported nanoparticles. This process is mostly induced by voltage cycling, which promotes the Pt nanoparticle dissolution and growth via electrochemical Ostwald ripening mechanism [5] and the precipitation of dissolved Pt^{2+} ions into the ionomer phase. Corrosion of the carbon support could occur [6,7] usually observed as loss of pores volume or electrode thinning. Also perfluorosulfonic acid (PFSA) membranes [8] and electrode ionomers [9,10] are subjected to degradation, because of radicals chemical attack or because of mechanical stress, both causing membrane thinning, loss of conductivity, mass transport alterations and even cell failure when pinholes and cracks are generated.

Under this complex scenario, the evaluation of durability is a clue topic for the technology. On one side, a reliable evaluation of PEMFC performance decay is fundamental to benchmark different materials and compare results from different laboratories. Besides, a reliable experimental evaluation

is also the key basis for developing prognostic methods which aim to predict systems lifetime. The most relevant metrics for assessing PEMFC performance and degradation are obtained operating Membrane Electrode Assemblies (MEA) in single cell configuration. However, since the abovementioned struggling durability targets, long-term and complete tests are not always feasible. To overcome this issue, accelerated ageing protocols are usually exploited, alternated to periodic performance testing and diagnostics. These are named as Accelerated Stress Tests (AST) and in the past many different protocols were proposed, most of them aiming to provide a rapid evaluation of cathode electrocatalyst durability [11,12]. Over the years, however, the protocols adopted by the U.S. Department of Energy have become the most recognized reference ASTs to selectively evince the stability of *i*) Pt/Pt-alloy catalyst, *ii*) the catalyst carbon support and *iii*) the membrane, in an independent way [13,14] Even though the importance of identifying specific component alterations for R&D purposes, the correlation between AST degradation and the real ageing is still a critical objective to fulfil [15,16]. On one hand, direct correlations are not possible since multiple degradation mechanisms simultaneously occur in automotive driving, superimposing one to each other. On the other hand, the transfer of the results is complicated by the presence of mitigation strategies on vehicles. Such strategies limit the operating voltage range of the system [17], as well as they accurately control the start/stop procedures, avoiding both open circuit voltage (OCV) and air leaks into the anode compartment [18,19].

The purpose of this work is to define ASTs representative of automotive operations [20] that can be exploited for predicting real MEA degradation and thus complimentary to the existing protocols. To reach this aim, an approach for the ASTs design is presented, which consists in starting from operating conditions and load cycles close to real-world. As the name says, an AST must accelerate degradation to keep the total testing time to reasonable values; however, the laboratory protocol must also promote ageing phenomena analogous to those involved in real operations if it would be claimed as representative. Operational mode ASTs are here defined such to replicate low power and high power modes of functioning. These “single mode” ASTs are joined together to mimic all the drive cycle ageing stressors in what is called as “Combined AST”. The results of this new AST are compared to the single cell long-term and complete ID-FAST dynamic load cycle protocol (indicated as DLC in the following) [3], to verify the consistency to real ageing.

Reliable degradation studies require also testing hardware that must minimize their influence on the MEA ageing protocol results. Any kind of interdependence, as the flow field design, must be avoided if the inherited CCM durability is the focus of the investigation. This work adopts a zero-gradient hardware, developed from a previous version [21], that permits the simultaneous testing of a few CCMs. The purpose of such a hardware is to ensure uniform operating conditions, accurately

controlled. In addition, the *open source* hardware [22] could be exploited for mimicking the local behaviour of PEMFC under realistic conditions, which are by nature heterogenous.

This work is organized as follows. In the Experimental section we introduce the experimental *in situ* and *operando* techniques adopted for analyzing PEMFC degradation. Detailed paragraphs are devoted to the description and the reasoning under the new AST protocols design. The outcomes, consisting of both novel AST predictions and validation against single cell DLC ageing, are presented in the Results section. The Conclusion section summarizes the main findings. The presented rigorous methodology of this paper for AST design, validation and degradation mechanisms investigation has the potentiality to be generalized to other automotive load profiles, in case different system mitigation strategies would be mimicked.

3. Experimental methodology

3.1. Material and ex situ characterization

The experimental analysis was performed on three types of MEAs. Each MEA consist of a Catalyst Coated Membrane (Pt/C both at anode and cathode) and gas diffusion layers (Freudenberg GDL H14CX483). Three CCMs (named A, B and C) were adopted and supplied by different manufacturers. The choice of repeating the degradation analysis for different commercial CCMs aimed at proving the validity of the developed methodology. Specific additional investigations were carried out for CCM B since it resulted as more promising in terms of performance stability. The compression of the samples was set to 81%, for CCM A and CCM C, and to 80% for CCM B by using rigid gaskets in Mylar®. Samples characteristics are summarized in Table 1.

Table 1 Characteristics of the tested CCMs tested either declared by the manufacturers or obtained through SEM images.

Characteristic	Units	CCM A	CCM B	CCM C
Cathode Catalytic Loading	[mg cm^{-2}]	0.4	0.5	0.4
Anode Catalytic Loading	[mg cm^{-2}]	0.08	0.1	0.1
Membrane thickness	[µm]	15	18	18
Cathode Catalyst layer thickness	[µm]	10	15	10
Anode Catalyst layer thickness	[µm]	7	5	3
Carbon support		graphitized	graphitized	-

A microstructural characterization of fresh and aged CCM B samples was carried out using scanning electron microscopy (SEM) and transmission electron microscopy (TEM) techniques. SEM and TEM observations were respectively performed using a ZEISS-MERLIN field emission gun (FEG) microscope and a FEI-Titan Ultimate microscope equipped with both a Cs aberration probe and image corrector. For SEM observation of the MEA cross-sections, the samples were embedded in epoxy

resin and mechanically mirror-polished whereas for TEM analysis 100 nm-thick slices were obtained using a LEICA ultramicrotome. Histograms of Pt nanoparticle (Pt NP) size distribution were built from TEM images, after a manual measurement of spherical nanoparticles diameters. Only spherical and not agglomerated particles have been considered into manual counting. Pt NP histograms were used for the calculation of the average volume/area diameter $\bar{d}_{v/a}$ [23], from which the Geometric Surface Area (GSA) is quantified according to Equation 1:

$$GSA\left[\frac{m^2}{g}\right] = \frac{6}{\rho_{Pt}}\frac{\sum_i d_i^2}{\sum_i d_i^3} = \frac{6}{\rho_{Pt}}\frac{1}{\bar{d}_{v/a}} \quad (1)$$

When referring to $\bar{d}$ instead, the quantity represents the number averaged diameter computed as the arithmetic mean $\sum_i d_i \,/\, n$, where n is the number of counted nanoparticles.

3.2. Hardware and setup

The work adopts a novel zero-gradient cell hardware, developed at Politecnico di Milano from a previous version [21], to operate the MEAs in homogeneous conditions over the cell area. The new design consists in a segmented version of the *open source* zero-gradient cell, the geometry and the drawings of which are detailed in the related work [22]. The hardware, which plate is divided into four parts, allows the testing of four 2 cm^2 MEAs simultaneously. It is therefore a useful solution for testing more materials for validation and repeatability purposes, as included in this publication. The cell hardware is characterized by a parallel flow field and high stoichiometry ratios are used, equivalent to 8 and 20 at anode and cathode respectively, which were defined consistently with the assumption of a zero-gradient hardware.

The experimental setup is schematized in Figure SI-1. The gas flow rates are supplied through mass flow meters (Brooks® 5850s) and humidified by water bubblers (Fuel cell tech®), of which the dewpoint is directly controlled. Prior the cell manifold, heated ducts are placed to avoid water condensation. At the cathode size, two three-way valves are introduced. The first one allows to switch from humidified air supply to dry air supply (0% RH), bypassing the bubbler. The second is instead useful for implementing the short stop procedure, the details of which are included in the Supplementary Material. This second valve is used for preventing air leakages from the bubbler during such short stop protocol, that comprises no cathode feeding by completely closing the cathode manifold inlet section. Reactants pressure is regulated at the cell inlet using electronic controllers coupled to backpressure valves (Equilibar® LF Series). Pressure transducers (GE® Unik 5000) are installed at inlet while the differential pressure is measured between inlet and outlet, upstream and downstream the manifolds of the hardware. A multichannel 63610-80-20 Chroma® electric load

allow to operate the different MEAs in an independent way both during the AST protocol application and during polarization curves measurements. For specific *in-situ* electrochemical diagnostics, an Autolab® potentiostat is used. Protocols are developed in LabView® interface, while data acquisition is based on National Instrument® DAQmx interface.

3.3. Break-in procedure

The break-in protocol is applied to all the tested MEAs. It is carried out at 65 °C, 100% RH and ambient pressure, while the current density set points are switched every 2 minutes between 0.2 and 0.8 A cm^{-2} for a total of 17 hours as already reported in works [3,21].

3.4. In situ characterization

3.4.1. Voltammograms, Polarization Curves and Limiting Current

During the hydrogen/air ASTs, the design of which is specified in the protocol section, the MEAs were electrochemically characterized in regular intervals through polarization curves, electrochemical impedance spectroscopy (EIS), cyclic voltammetry (CV), linear sweep voltammetry (LSV) and limiting current measurement for oxygen mass transport quantification. The ECSA was calculated by the H-desorption area of CV, as an average on four scans, assuming a specific charge of 210 μC cm^{-2}. The voltammograms were recorded between OCV and 0.6 V with H_2-rich anode as reference electrode, at the scan rate of 100 mV s^{-1}, at 30 °C and providing fully humidified H_2/N_2 flows, both equivalent to 0.1 NL min^{-1}. LSV was used for estimating hydrogen crossover: i-V quantities were linearly correlated and the value of current density extrapolated at null voltage. LSV was recorded between 0.05 V and 0.6 V with a scan rate of 1 mV s^{-1}, 80 °C and fully humidified gases, both at ambient pressure and at pressure conditions equivalent to those used for evaluating the limiting current, reported in the following. The inverse of LSV slope in the range between 0.3 V and 0.6 V provides instead an estimation of the electronic shorting resistance.

The limiting current test was designed starting from a literature approach [24]. Three dilutions were tested: 1%, 2% and 3% of $x^{dry}_{O2,in}$ in nitrogen, at pressures $p_{A,in/C,in}$=170/150 kPa, 270/250 kPa, 370/350 kPa. Hydrogen flow was kept constant at 1.0 NL min^{-1}, while cathode flow at 4.0 NL min^{-1}. The cell voltage was held for 3 minutes at 0.4 V, then held for 3 minutes each at 0.3 V, 0.2 V and 0.1 V, at which potentials the limiting current was recorded and averaged over the time. The oxygen mass transport resistance ($R_{MT,O2}$) was computed according to Equation 2:

$$R_{MT,O2} = 4F \frac{x_{O_2}^{dry}}{i_{lim,measured} + i_{crossover}(p_{H_2})} \frac{p - p_w}{RT} \quad (2)$$

Where x^{dry}_{O2} is the oxygen molar fraction, computed as the logarithmic average between inlet and outlet. The outlet mole fraction is estimated considering that part of oxygen is consumed because of the drawn current [3].

Performance evolution during the protocol application was monitored through polarization curves. Each current density of the polarization curve was held for 180 s and averaged over the last 120 s, considering the progress from high to low currents. Polarization curve operating parameters are equivalent to 80 °C, fully humidified gas feedings, $p_{A,in/C,in}$=250/230 kPa, stoichiometry equivalent to 8/20 at anode and cathode respectively. Under the named "reference conditions", gas feedings are hydrogen and air. The same operating parameters have been also exploited for carrying out a pure oxygen polarization curve, fixing the same flow rate as in the air polarization, thus increasing the oxidant stoichiometry by approximately a five factor. EIS was measured in galvanostatic mode at 2 A cm^{-2}. A total of 50 frequencies was applied, in the range from 50 mHz to 20 kHz. Oxygen reduction reaction mass activity was computed from the oxygen polarization current density at 0.9 V from the Tafel plot (semi-log plot of voltage with respect to current density), and normalized to the initial Pt mass in the cathode catalyst layer. Note that the cell voltage was corrected for the high frequency resistance (ohmic contribution), while the current density was corrected for the hydrogen crossover.

3.4.2. Correlating Zero-Gradient hardware degradation to standard single cell

The zero-gradient hardware is used for developing and performing the Accelerated Stress Tests. The degradation induced by the novel ASTs is then compared to the long-term single cell DLC included in a previous work [3], with the aim of providing validation over realistic automotive-like data. However, this validation requires to compare the performance evolution on two different hardware setups (*i.e.* Zero-Gradient and standard 25 cm^2 triple-serpentine single cell). To make such a comparison consistent, current density values were selected in order to satisfy the criterion of identical Beginning of Test voltage under the reference operative conditions (see Table 2). Note that values at 0.78 V are very close for the compared hardware while discrepancies rise at 0.65 V, where the current density is significantly higher for the Zero-Gradient cell because of its concept design and the larger stoichiometries adopted [22,25,26]. The current densities correspondent to a BoT cell voltage of 0.78 V (low current, named setpoint 1) and 0.65 V (high current, named setpoint 2) are thus exploited in the Results section for tracking the performance evolution during the degradation protocols.

Table 2 Current density setpoints for the tested CCMs, selected in order to guarantee the voltage value of 0.78 V and 0.65 V at the Beginning of Test (BoT), specific for the hardware. Reference operative conditions are considered (80 °C, fully humidified gas feedings, $p_{A,in/C,in}$=250/230 kPa and λ_A/λ_C = 8/20 for Zero-Gradient, while λ_A/λ_C = 2/4 for the 25 cm² triple-serpentine single cell). Setpoints are used to compare the voltage loss evolution over time in case of protocols applied on different hardware setups.

hardware	BoT voltage (reference operating conditions)	Current density name	CCM A	CCM B	CCM C
Zero-Gradient cell	0.78 V	Setpoint 1 (low)	0.8 A cm^{-2}	0.7 A cm^{-2}	0.7 A cm^{-2}
	0.65 V	Setpoint 2 (high)	2.9 A cm^{-2}	2.8 A cm^{-2}	2.9 A cm^{-2}
25 cm² triple-serpentine single cell	0.78 V	Setpoint 1 (low)	0.7 A cm^{-2}	0.7 A cm^{-2}	0.6 A cm^{-2}
	0.65 V	Setpoint 2 (high)	1.6 A cm^{-2}	1.9 A cm^{-2}	1.9 A cm^{-2}

3.5. DoE Electrocatalyst AST protocol

The U.S. DoE Electrocatalyst AST [13] consists of potential cycling between 0.6 V and 0.95 V at 3 s holding time each for a total of 75'000 cycles. It was conducted in H_2(anode)/N_2(cathode) at 0.1 Nl min^{-1}, at 100% RH (both sides) and atmospheric pressure. Potential is changed at a scan rate of 0.7 V s^{-1}.

3.6. Design methodology for automotive single "mode" AST protocol

This section describes the methodology adopted for designing automotive single mode Accelerated Stress Tests, consisting in Low Power AST (LP-AST) and High Power AST (HP-AST). These new single mode ASTs for Zero-Gradient hardware aim at reproducing realistic (*i*) operating conditions (as temperature and pressure), (*ii*) voltage cycling and (*iii*) MEA humidification state, in order to stay as close as possible to automotive operations. The choices were carried out based on the single cell ID-FAST DLC [3]. Since the AST implementation must be accurate but also easily reproducible, the following requirements were thus defined:

(i) Regarding operating conditions, fixed parameters as cell temperature and mass flow rates were selected. Flow rates for zero-gradient hardware were set to be equivalent to the stoichiometry of 8/20 at the maximum AST current density setpoint, for anode and cathode. The average conditions of an MEA subjected to DLC were reproduced by selecting operating parameters that would mimic its middle region, proved to be sufficiently representative of the overall single cell behaviour (Figure SI-2);

(ii) A load profile under hydrogen/air was applied by varying the current density (constant current operation). Current densities were defined in order to mimic the Beginning of Life performance in terms of cell voltage. A realistic voltage window and a realistic number of potential transitions were adopted in the design, as specified later in Sections 3.6.1 and 3.6.2 and shown in Figure 1. Pressure cycling occurs during the short stop which was introduced every AST cycle (both LP and HP) and consisted in stopping the air flux, while still supplying hydrogen at the anode. Cathode pressure was thus reduced to ambient, while the absolute anode pressure was decreased to a minimum of 150 kPa. A resistive control made the voltage decline from 0.85 V to very low values (<0.1 V), since all the oxygen at cathode was progressively consumed. At the same time, OCV was avoided as in the applications. The introduction of this stop procedure was fundamental to cover all the potential variations that are expected in automotive systems [17] at a realistic frequency [4];

(iii) Third, for estimating the MEA humidification state, the High Frequency Resistance at 1k Hz was used as an indicator, the dynamics of which is tracked in *operando* (Figure 1).

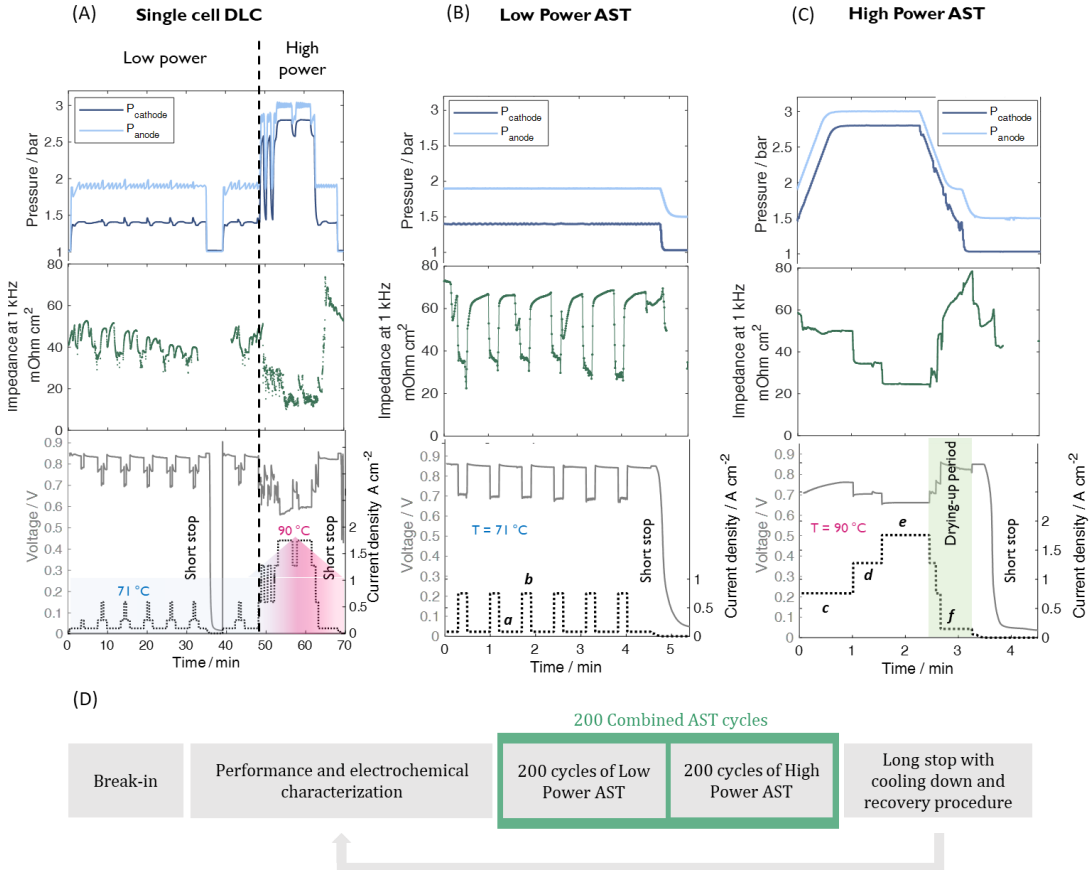

Figure 1 (A) Operating parameters applied during each cycle of the single cell ID-FAST DLC protocol [3]*: outlet pressures (expressed as absolute values), measured high frequency resistance, current densities and cell voltage profile at BoT. Two short stops are introduced every operating hour; (B) Design of the Low Power AST. Applied current profile (values are for CCM B) and pressure cycles. Measured cell voltage and high frequency resistance at Beginning of Test; (C) Design of the High Power AST. Applied current profile (values are for CCM B) and pressure cycles. Measured cell voltage and high frequency resistance at Beginning of Test; (D) Scheme of the novel Combined AST protocol*

A combined AST is finally defined in Section 3.6.3 to be compared with the degradation observed under the DLC protocol including the full driving cycle.

3.6.1. Low Power AST

The Low Power AST (LP-AST) protocol consists in applying an accelerated version of the load profile defined as the automotive low power operation. The operating parameters of Low Power AST and the protocol details are included in Tables SI-1, SI-2 and SI-3. In brief, the cell temperature is set at 71 °C, while the inlet pressure controlled to be equal to 140 kPa/190 kPa at cathode and anode respectively. Average dew points were estimated equivalent to 63.2 °C at cathode and 59.1 °C at anode, equivalent to a relative humidity of the gas feedings of 71% and 59% respectively. The original design of the long-term protocol, depicted in Figure 1.A, is accelerated by a x7 factor on the operative time basis. The acceleration consists in reducing the dwell times while keeping a realistic number of potential transitions and the system operational voltage window. In particular, the maximum voltage was not exacerbated to avoid non-realistic degradation mechanisms. The acceleration factor was defined according to literature review and through some attempts that finally led to this choice, that is a compromise between acceleration and representativeness. Indeed, literature recognizes that potentiodynamic processes are clue for electrocatalyst ageing, proving that Pt nanoparticle size growth occurs more rapidly while cycling [27], since the electrochemical Ostwald ripening mechanism is strictly related to the oxidation state of the catalyst surface [28]. Zihrul et al. [29] showed that the holding time at high potential impacts less than the maximum voltage value: the difference in catalyst active area loss diminishes at increasing holding time because a near steady-state surface oxide coverage is probably reached. The work of Kneer et al. [30] attributed instead a more relevant role to the time spent at high voltage, evidencing that the ECSA loss per cycle is more severe for longer cycles when testing a holding range of 4 s – 600 s; however, the major differences were evinced in the window 4 s – 60 s. Starting from these information and from our findings (see Figures SI-3 and SI-4), a final holding time of 30 s was selected for the highest potential in this work.

A single low power AST cycle is formed by a basic unit of 30 s at low current (*i.e.* 0.85 V at BoT) and 12 s at high current (*i.e.* 0.7 V at BoT); the basic unit is repeated 6 times and it is finally followed by 30 s at low current, after which a short stop of 110 s is introduced (Figure 1.B). Since the cell voltage decreases to very low values during short stops because of air starvation, this procedure is expected to fully reduce the catalyst surface, interacting with the Pt dissolution mechanism and being thus relevant to mimic realistic ageing. In addition, the stop procedure is coupled to pressure cycles between 140 kPa and ambient pressure at the cathode side, while between 190 kPa and 150 kPa at the anode side.

3.6.2. High Power AST

In analogy with the previous section, the High Power AST (HP-AST) protocol is a load profile consistent with the automotive high power operation. Operating parameters and protocol details of the High Power AST are included in Tables SI-4, SI-5 and SI-6. Again, the middle region of an MEA operating under the DLC protocol is mimicked: in this case, the MEA temperature was kept constant and set equivalent to 90 °C. Absolute pressures are equal to 280 kPa/300 kPa (cathode/anode), but are reduced prior the stop to 190/140 kPa and then to 150/101 kPa during the short stop protocol. All these dynamics are depicted in Figure 1.C. Relative humidity of hydrogen is 59% at anode and is kept constant during the test. On the opposite, cathode dew point is not constant but air feeding humidification is cycled between 68% RH in the first part of the HP-AST to almost 0% RH starting at the 145th second. This is achieved by a gas switch from partially humidified to dry air and the scope is to reproduce the membrane hydration/dehydration cycles that are observed in the DLC. The original DLC design is accelerated by a x7 factor in operating time, as for the low load operation. The voltage encompasses four setpoints, defined as the current densities that correspond to 0.85 V, 0.75 V, 0.70 V, 0.65 V at BoT, consistently to those values expected in real systems (Figure 1.A). Changing simultaneously the current setpoint (from high to low values) and the humidification of cathode feeding (gas switch from humidified to dry air), the high frequency impedance of the realistic DLC operation is reproduced. Indeed, the MEA drying-out prior to stop, evidenced in Figure 1.A and due to the shift from high to low power demand under still hot conditions, is quantitatively well simulated, as included in Figure 1.C.

3.6.3. Combined AST

The Combined AST protocol aims at reproducing the ageing induced by full automotive driving. To reach this objective, the newly designed LP-AST and HP-AST are combined together in order to take care of the possible interplay between the two operational modes. The scheme of the Combined Accelerated Stress Test is reported in Figure 1.D. Blocks of 200 cycles of each single mode AST are carried out in a row, in order to ensure the alternation of operations but also to switch from low to high load conditions in a feasible way, since the protocols differ in operative parameters. In particular, the regulation of both cell and dew points temperatures between the set of LP and HP cycles is carried out under hydrogen/nitrogen. The accelerated durability test program was applied until reaching 1000 combined cycles (for a total of 1000 LP-AST cycles and 1000 HP-AST cycles), where a “combined cycle” is equivalent to the sum of 1 LP-AST and 1 HP-AST cycle. Characterization is regularly introduced after every 200th combined cycles and it includes the measurements reported in the *in situ*

characterization (Section 3.4.1). The test was then repeated on all the three CCMs to verify the results reproducibility and carried out till 2000 combined cycles to study the AST longer-term prediction.

4. Results and discussion

4.1. Reproducing automotive degradation mechanisms

4.1.1. Electrochemical Active Surface Area and Pt NP size distribution

The ECSA was used as a primary parameter to evince the catalyst degradation. It is fundamental for tracking the consistency of ageing and the acceleration factors of the three MEAs tested under both the Combined AST and the single cell DLC protocol.

The obtained ECSA decays under Combined AST are compared among the different tested CCMs in Figure 2.A, both as a function of cycle number which is proportional to the operating time. The Pt active surface area loss is largely promoted during the first 200 combined AST cycles. After the initial high drop, the intensity of which slightly depends on CCM type (*e.g*. greater for CCM B than C, being equivalent to 30% and 24% respectively), the subsequent rate of decay strongly decreases. In the range 400-1000 cycles, the ECSA varies of just 7%÷12%, leading to a final value at 1000 combined AST cycles of 61%, 63% and 65% of retained ECSA for CCM A, B and C respectively.

SEM and TEM analysis were performed on the aged CCM B. SEM image in Figure 3.F shows that no Pt band is formed in the membrane after the operation under hydrogen/air. On the other hand, TEM image in Figures 3.C and 3.D clearly illustrate the very large increase in Pt NP size consequent to dissolution and re-deposition, proving that the electrochemical Ostwald ripening is the most promoted mechanism responsible of catalyst ageing. TEM analysis allowed also to reconstruct the particle size distribution histogram of Figure 3.B, for which a large number of nanoparticles, as included in Table 3, was considered. The average volume/area diameter increased from 4.8 nm to 7.3 nm and the catalyst utilization factor (*i.e*. the ratio between the geometric surface area computed from between the GSA and the ECSA) undergoes just minor changes with ageing, from the initial 68% to the final 72% value.

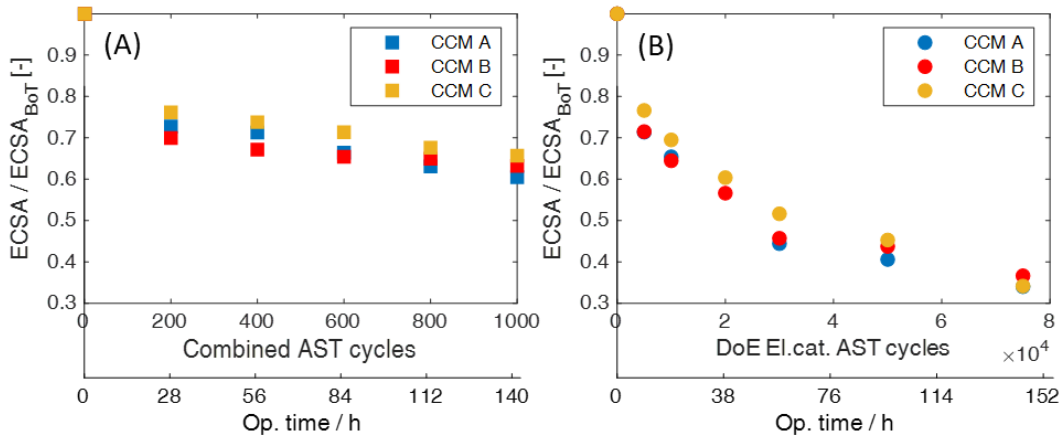

Figure 2 (A) ECSA evolution: comparison among different CCMs under Combined AST as a function of combined cycles and operating time; (B) ECSA evolution: comparison among different CCMs under the Electrocatalyst AST as a function of cycles and operating time.

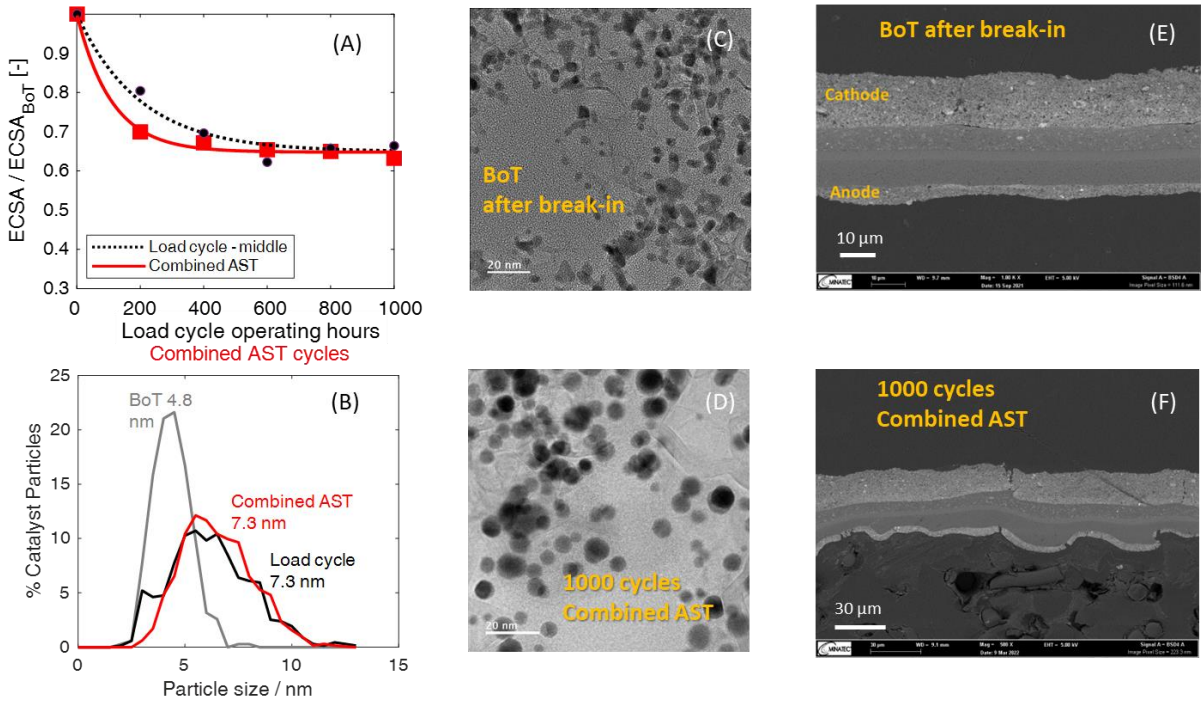

Figure 3 (A) ECSA evolution: comparison between Combined AST and DLC protocol in the MEA middle region (seg2, empty dots, and seg 3, full black dots) reproduced from the previous work [3] *for CCM B. Fitted line is also included; (B) Pt NP size distribution of CCM B at BoT, after break-in procedure, and after the application of 1000 cycles of Combined AST (in red) and after 1000 operating hours of DLC protocol for the MEA middle region* [3]*. Note that the size reported is the average volume/area diameter;(C) TEM image of CCM B after the break-in protocol application.; (D) TEM image of CCM B after the application of 1000 Combined AST cycles; (E) SEM image of CCM B after the break-in protocol application; (F) SEM image of CCM B after the application of 1000 Combined AST cycles. PEM and electrodes deformation is visible, as well as some cracks.*

Table 3 Summary of TEM images analysis results, carried out for CCM B, both after break-in and for the MEA aged under 1000 Combined AST cycles. Information is also compared to the air-middle location of the MEA aged under 1000 operating hours of drive load cycle protocol(*)[3]*. The table includes counted particles, the geometric surface area and average volume/area diameter. Results are compared to ECSA and catalyst roughness factor evaluated by Cyclic Voltammetry.*

CCM B protocol	Counted particles [-]	$\bar{d}$ [nm]	$\bar{d}_{v/a}$ [nm]	GSA [m^2/g]	ECSA [m^2/g]	Catalyst roughness factor [cm^2_{Pt}/cm^2_{geo}]	ECSA loss [%]
After break-in	347	4.4	4.8	58.7	40.1÷41.5	201÷208	-
1000 hrs of single cell drive load cycle DLC (middle region)(*)	672	6.2	7.3	38.4	26.3	131.5	34.4
1000 cycles of Combined AST	613	6.5	7.3	38.3	27.5	137.5	36.8

The evolution of ECSA during the Combined AST is studied in comparison to evolution observed in the Electrocatalyst AST (Figure 2.B), selected as a reference since it is the most commonly adopted AST for testing the cathode electrode durability. The loss of ECSA in time is more promoted by Electrocatalyst AST, that encompasses square wave cycles in the potential range between 0.6 V and 0.95 V. In the novel AST instead, the potential never exceeds 0.85 V, consistently with operating strategies that avoid OCV condition. As expected, limiting the maximum voltage leads to a lower rate of decay. Other factors, as the lower temperature and the lower relative humidity, can inhibit the degradation too. It is also noteworthy that the Combined AST avoids the dissolution and the reprecipitation into the membrane at all, as confirmed by the absence of Pt band. At the opposite, literature works proved that the Electrocatalyst AST enhances such a process, identifying both Pt precipitated into PEM [31] and a Pt depletion zone [32,33] in the catalyst layer.

The novel Combined AST caused a catalyst degradation consistent with the drive protocol. Indeed, Figure 4.A-C shows the analogous ECSA decays confirming that 1000 cycles of Combined AST reproduce what happens during 1000 operating hours of realistic load cycling for all the CCMs. The Combined AST was carried out twice on all the samples, verifying the good repeatability of the protocol. The two profiles obtained from the repeated protocol deviate for a maximum percentage of retained ECSA that is within the ±5%, ±1% and ±2% for the three CCMs, in the order A, B and C. On the other side, Electrocatalyst AST, which evolution of ECSA was reported in Figure 2.B does not reproduce the evolution of ECSA observed in the DLC, supporting the necessity to develop new AST protocols that are more representative of the real-world ageing.

In addition to ECSA, also the Pt NPs histograms of the aged CCMs agree very well (Figure 3.B). The initial narrower Pt NPs distribution became more widespread in the range 3-12 nm in a highly

consistent way, in spite of the presence of a group of smaller particles in the drive protocol. It is speculated that this group (d < 3 nm) might be a characteristic of the specific sample, possibly not contacted by the ionomer and therefore not taking part into the dissolution mechanism. The calculated GSA decreased from 58.7 m^2g^{-1} to 38.4 m^2g^{-1} in case of DLC and to 38.3 m^2g^{-1} in case of Combined AST, correspondent to an average volume/area diameter equal to 7.3 nm in both the cases.

The very good agreement allows to conclude that the main drivers that control the Pt catalyst ageing under the automotive load cycle have been correctly reproduced by the Combined AST. These results are consistent with the fact that the electrochemical Ostwald ripening mechanism, once selected representative temperature and relative humidity, is mainly governed by the potential limits and it is strictly connected to the oxidation state of Pt surface. This work proves the efficacy of the illustrated approach based on (*i*) setting the same number of potential transitions between the minimum and the maximum voltage, kept in a representative voltage window; (*ii*) exploiting lower dwell times, where the linear time reduction is a trade-off between the testing acceleration and the necessity of obtaining a representative interaction between Pt oxides growth and Pt NP dissolution.

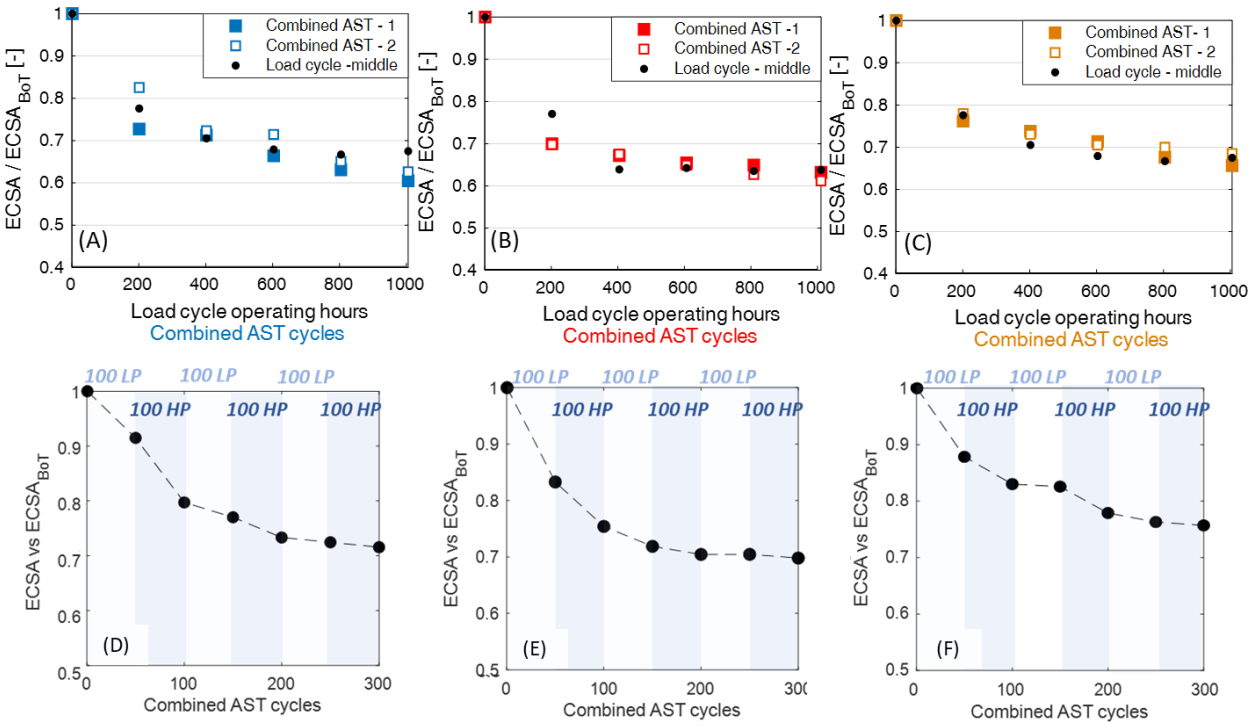

Figure 4 ECSA decay profiles under the Combined AST protocol application, applied till 1000 cycles (Combined AST – 1 and repeated Combined AST – 2). The profiles are compared against the drive load cycle protocol for the middle region (seg 3 included in a previous work[3]*). Value are reported for CCM A (figure A), CCM B (figure B), CCM C (figure C); Detailed ECSA evolution under Combined AST application. ECSA is detected every 100th cycles of Low/High Power AST. The protocol is carried out for a total of 300 combined cycles on CCM A (figure D), CCM B (figure E) and CCM C (figure F).*

4.1.2. Focus on the initial loss of Electrochemical Active Surface Area

As previously observed, the largest drop of Pt active surface area is promoted during the first 200 Combined AST cycles. The Combined AST was therefore repeated with the purpose of better

describing the very initial degradation of catalyst met during operation. A testing protocol based on alternating 100 cycles of LP-AST and 100 cycles of HP-AST was applied on all the CCMs. This specific study was limited to a total number of 300 combined cycles, but it was committed to a much more frequent characterization. As evinced in Figure 4.D-F, the largest initial drop could be restricted to the first 100 combined cycles. After 100 combined cycles only, the retained ECSA is the 80%, the 75% and the 83% for CCM A, B and C respectively. This additional experimental campaign highlighted also the specific role of low load and high load operation. It is worth mentioning that even the very first 100 cycles of low power are clue in degrading the cathode electrode catalyst, even though it is difficult to assess if one kind of process impacts more than the other. Indeed, in spite of the different operating conditions of the two protocols, the single contributions seem to follow a shared decreasing profile.

4.1.3. Voltage loss analysis and microstructural changes in the electrode

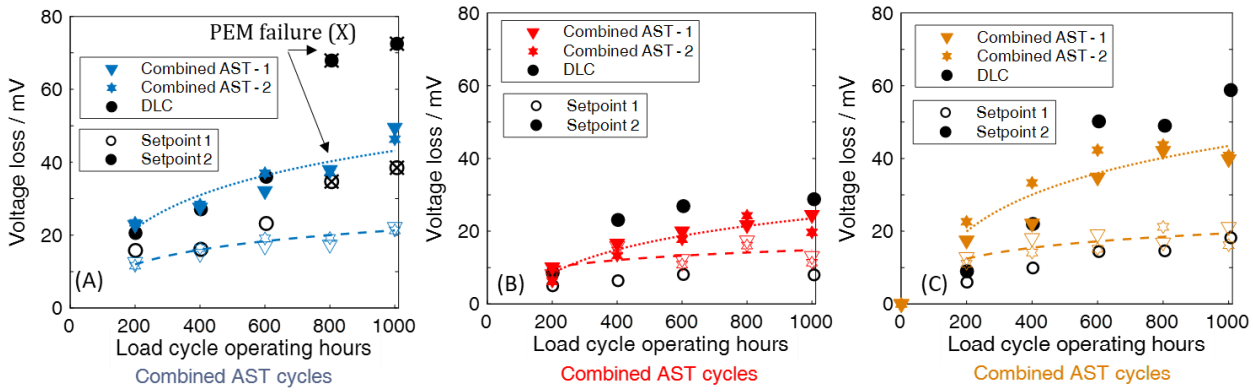

Figure 5 Voltage losses due to Combined AST (coloured), repeated twice, computed for setpoint 1 (empty symbols) and setpoint 2 (full symbols) as a function of the number of AST cycles. See Table 2 for setpoints description. Results are compared against the average cell voltage losses induced by the drive load cycle (DLC, black) over 1000 real operating hours. Values for the all the three tested MEAs are included: CCM A (figure A), CCM B (figure B) and CCM C (figure C). Dotted lines are just guide-to-eye, identified as logarithmic trends of the average Combined AST losses.

In addition to ECSA, the irreversible degradation of each test was tracked by evaluating voltage losses. Performance evolution was described through two setpoints, named as setpoint 1 (low current) and setpoint 2 (high current) obtained from reference polarization curves and selected as discussed in the Experimental section.

The voltage loss caused by the Combined AST is depicted in Figure 5. The protocol, carried out twice for each CCM, shows a good repeatability, as already evinced for ECSA decay. The voltage loss of the two repeated test differed within the measurement uncertainty, being included in a band within ±2 mV for both CCM A and CCM B and ±6 mV for CCM C. In the same Figure 5, the voltage loss due to DLC protocol is included too. First, the Combined AST protocol is able to rank the CCMs. CCM B ended as the most resistant. Voltage losses at setpoint 1 are very well reproduced in all the

cases, as expected since the comparable Pt active surface area decay: at low currents, the decrease of performance is mainly related to reactions kinetics. At the opposite, gas transport limitations become more relevant at increasing values of geometric current densities [34], that is the case of setpoint 2. At this current, the performance losses are slightly underestimated for CCM B and CCM C for a high number of cycles, but the overall trend of the real-world ageing is correctly captured by the AST protocol. The differences could be attributed to the fact that the implemented AST is mimicking the local degradation of the middle region and it does not account for the effects of heterogeneity of ageing. In particular, it has been demonstrated that DLC promotes larger mass transport limitations at the air inlet region [3], being detrimental at high loads. Anyway, the Combined AST is able to provide an effective and quantitative brief picture: the largest losses are detected in the first 200-400 cycles, after which the rate of decay is reduced and the tendency is towards a progressive stabilization. Note that the voltage losses of CCM A diverge as the membrane failed under the DLC protocol. Nonetheless the absence of failure in the proposed Combined AST, the protocol was able to differentiate between PEMs characterized by different mechanical properties through the detection of changes in shorting resistance. The short circuit resistance of the membrane for CCM A is reduced to the 50% of the initial value at 1000 cycles, capturing the lower resistance of the membrane of this sample (Figure SI-5). The reduction indicates a probable localized thinning. At the opposite, no evident changes of HFR have been detected (Figure SI-6). The other MEAs show lower shorting variations, in the range of 80%-110% compared to BoT values. Furthermore, microstructural changes in the electrodes and membrane were observed too, consistently to DLC observations [3]. It is remarkable that deformations of both membrane and electrodes are already visible after 1000 combined cycles, as well as some cracks (Figure 3.F). They might be the result of ionomer mechanical stress, enhanced by water content oscillations [35] coming from load, pressure and dew point cycling (wet-dry air).

4.2. Analysis of MEA performance decay

4.2.1. Cycle efficiency and power loss

The performance of PEMFC is monitored during operation through the fuel cell output power. This parameters evolves in time because of reversible and irreversible ageing mechanisms [36], the interplay of which could not be neglected when assessing how real systems would respond. Some processes that allow the recovery have been reproduced, as the frequent short stops that ensure the removal of Pt oxides, which otherwise inhibit the oxygen reduction reaction [37]. In addition, long stops and recovery procedure (see Supplementary Material for details) where replicated every 200th combined cycles, guaranteeing CCM rehydration and possible contaminants removal.

The results at the minimum and at the maximum load are included in Figure 6.A and Figure 6.B respectively and an indicative *operando* degradation rate is provided by a simple linear fitting of the power curve. The degradation rate increases with the power value for all the tested CCMs, indicating that ageing impacts more on the high load operation rather than on low [38]. Differences in the provided power could be ascribed to CCM peculiarities. It is observed that, in spite of the lower performances at BoT, CCM B is the most stable, with a power decay equal to -11 and -65 μW cm^{-2} $cycle^{-1}$ for the minimum and the maximum load setpoints (0.080 A cm^{-2} and 1.76 A cm^{-2} respectively). CCM C suffers more at high load registering a drop of -78 μW cm^{-2} $cycle^{-1}$, consistently to the voltage loss analysis included in the previous paragraph. On the other hand, CCM A shows the largest rate at minimum load (-22 μW cm^{-2} $cycle^{-1}$), which is probably influenced by the worse mechanical properties of the membrane of this sample: the shorting resistance decrease (Figure SI-5) is indeed playing a major role at high voltage.

Low power and high power efficiency (η) are defined as the ratio of the output energy to the lower heating value of the consumed hydrogen during each specific operational mode, according to Equation 3. This expression considers a 100% hydrogen fuel utilization, neglecting the contributions due to hydrogen discharged by the purge and the hydrogen crossover to the cathode:

$$\eta = \frac{\int \Delta V \; i \; dt}{\int \frac{i}{2F} M_m^{H_2} dt \; \cdot LHV_{H_2}} \qquad (3)$$

where ΔV corresponds to the cell voltage, i is the current density, M_m^{H2} is the hydrogen molar mass and LHV_{H2} is the Lower Heating Value of the fuel. The efficiency is evaluated over one cycle of either LP or HP-AST and its evolution reported as a function of the combined cycles number in Figure 6.C, that proves the very good agreement for all the materials. As expected, the efficiency is lower in the high power mode (initial value equivalent to 53÷55%) since it is severely affected by the cell voltage, that reaches values as low as 0.65 V. At the opposite, an efficiency close to 60% is enabled during the low power mode that encompasses cycling above 0.7 V. Then, the high power efficiency falls to 51÷52% after 1000 combined AST cycles, while the low power one drops to 56%. The profile shows a recovery every 200th cycles, where a long stop is mimicked and a recovery procedure applied allowing to discriminate, and to eliminate, that part of the loss that is reversible. Once removed, efficiency is recovered of about 0.5÷1%. The largest irreversible loss is instead identified at the beginning of the test; again, consistently to the analysis of ECSA, the largest decrease is within the first 400 cycles, after which the trend appears more stabilized.

Figure 6.D includes the information of the irreversible degradation only, already presented in the previous section. In this picture, the fuel cell performance is directly compared at two current setpoints as a function of the cathode catalyst roughness factor. This parameter indicates the active

catalyst surface area per geometric surface area (expressed as cm^2_{Pt} cm^{-2}_{geo}) and it is directly proportional to ECSA. In spite of some incentivized degradation phenomena for CCM C at high current densities, commented before, this outcome indicates that the main ageing mechanisms that drive the degradation are common for all the CCMs and consistent to DLC findings. This kind of analysis had been already reported in the literature as effective for the purpose of predicting voltage loss [39]. What provided in this work is specifically useful for quantifying the performance decay arising under an automotive-realistic load cycling by knowing the changes in the catalyst surface area.

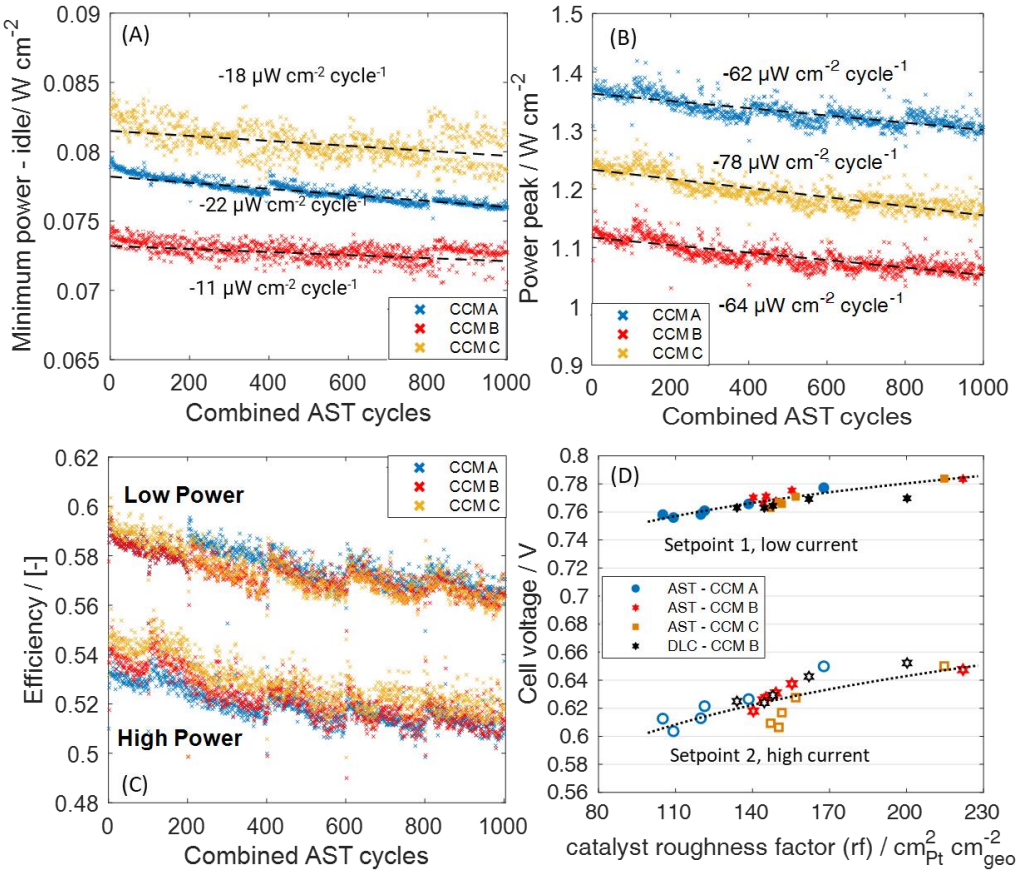

Figure 6 (A) Minimum power evolution for the three different CCMs under the Combined AST, evaluated at the current "a" of the protocol (see Figure 1.B); (B) power peak evolution for the different CCMs under the Combined AST protocol, evaluated at the current "e" of the protocol (see Figure 1.C); (C) Cycle efficiency computed according to Equation 3, computing considering the low power part and the high power part of the Combined AST protocol. Values are included for all the CCMs; (D) Measured cell voltage in reference polarization curve for two selected current densities (filled symbols setpoint 1 and open symbols setpoint 2, see Table 2 for load setpoints description) as a function of cathode catalyst surface over the course of Combined AST. Included logarithmic trends are a guide-to-eye, least-squares fitted over the experimental data.

4.2.2. The role of oxygen mass transport resistance

Oxygen transport resistance is measured according to the protocol described in Section 3.4.1 for the limiting current test. Determination of the limiting current density at various pressures allows to separate the overall oxygen mass transport resistance ($R_{MT,O2}$) into a pressure independent ($R_{MT,PI}$) and a pressure dependent component ($R_{MT,PD}$). Such quantities, determined at BoT and after 1000 combined cycles, are both included in Figure 7. Their values are obtained through a linear regression

of the $R_{MT,O2}$ data over the absolute cathode pressure (Figure SI-7); the slope of the linear fitting indicates how the resistance changes with pressure. The pressure dependent transport resistance, that comprises primarily the molecular diffusion in the large pores of the diffusion media GDL and partly MPL, is comparable at BoT for all the samples. Indeed, since the same GDL is adopted for all the tested MEAs, a value of 0.36 ± 0.02 s cm^{-1} is initially obtained at the pressure of 150 kPa. Such quantity basically did not vary after the protocol application, indicating no alterations of the GDL component. The output describes what happening in the real-world DLC, which caused the solely increase of the pressure independent resistance [3]. This contribution could be associated to the local thin-film oxygen transport resistance [40], due to CL ionomer ($R_{PI,ion}$), or to the Knudsen diffusion in the smallest pores of the electrode and MPL ($R_{PI,gas}$), as expressed by Equation 4 [34]:

$$R_{PI} \approx R_{PI,gas} + R_{PI,ion} = R_{PI,gas} + \frac{R_{local}}{rf} \quad (4)$$

Both the initial values and the increase of the pressure independent resistance are not identical for the different CCMs. CCM A evidenced an increase 1.5 times larger than CCM C, while CCM B showed the lowest growth of this quantity (~10% lower than CCM C). The $R_{PI,ion}$ component was calculated as the ratio between the local resistance and the roughness factor, according to Eq. 4; the local oxygen mass transport resistance was determined by plotting $R_{MT,O2}$ with respect to the inverse of the roughness factor (Figure SI-8). Other researchers [41] found a linear increase of the pressure independent resistance for low platinum loading PEMFC, which is attributed to an increased oxygen flux across the ionomer thin-film covering the platinum nanoparticles, consequence of the reduced available Pt surface area. The $R_{MT,O2}$ ageing induced by the Electrocatalyst AST was proved to be reasonably consistent to the effect of electrodes at reduced loads (as-prepared electrodes) [42]. The quantified values of mass transport resistance in the Electrocatalyst AST are included in Figure SI-8 as well: the R_{local} contribution was quantified as 10.7 ± 0.4 s cm^{-1}, 12.2 ± 0.1 s cm^{-1}, 13.3 ± 0.8 s cm^{-1} for CCM A, B and C respectively. This result is consistent to other author findings that obtained a value close to 12 s cm^{-1} for solid carbon support [42,43]. The Electrocatalyst AST was therefore adopted as a term of comparison for understanding the degradation occurring under the new accelerated protocol. A linear correlation is identified also for the Combined AST (Figure SI-8 and Table SI-7). However, in this new case, the Pt roughness factor decreases most at the beginning and then undergoes just minor modifications, as seen for the ECSA decay shown previously in Figure 2. In spite of the progressive stabilization of the Pt active surface area, the mass transport resistance continued to slightly grow leading, in the end, to a rate of increase with respect to rf^{-1} that is larger than Electrocatalyst AST. In particular, CCM C has the highest slope, equivalent to 17.2 ± 2.2 s cm^{-1}. Such higher value contributed to the lower CCM C performance at EoT. The result is also consistent

with the DLC observations [3] that highlighted the highest local resistance contribution of this CCM. At the opposite, CCM B slope is the lowest under Combined AST (15.7 ± 2.0 s cm^{-1}) and comparable from a quantitative point of view to DLC finding (15.9 s cm^{-1}). According to the described results, the new Combined AST is able to put in evidence those CCMs that are suffering most from mass transport limitations under the automotive dynamic load cycling. Underlying phenomena responsible of these alterations are proved to be related to pressure independent mechanisms and are likely attributed to the local thin-film resistance. The properties of ionomer in the cathode catalyst layer are thus suspected to be altered, maybe its distribution and contact to the catalyst [44]. Another possible contribution could come from the final electrode structure, as due to geometric-like effects caused by a heterogeneity in the dispersion of Pt nanoparticles [45], that is consequence of the catalyst ageing process.

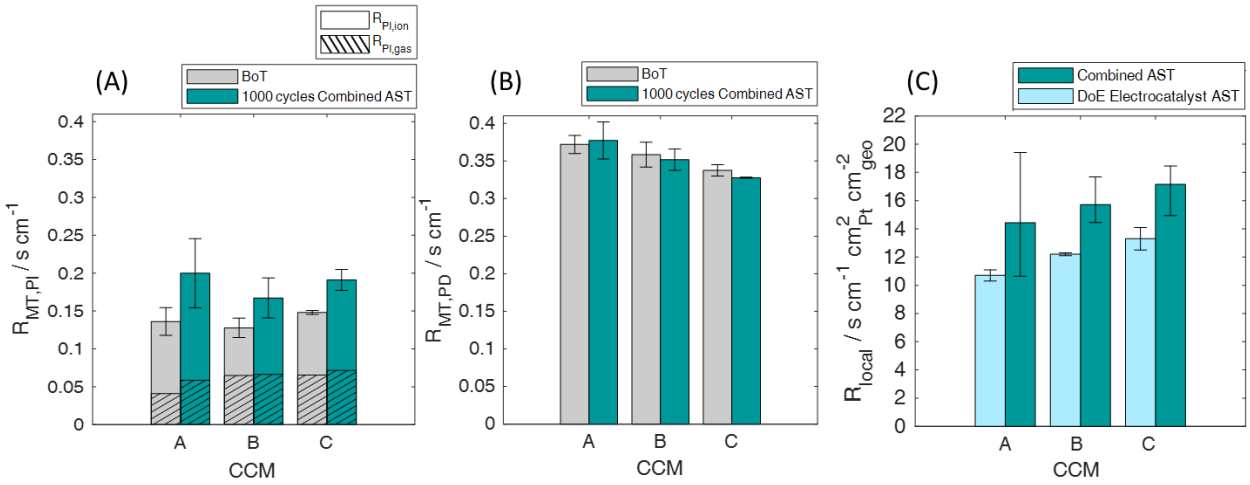

Figure 7 (A) Pressure independent (non-Fickian) component of the mass transport resistance evaluated at BoT and after 1000 cycles of Combined AST for the three different tested CCMs. The contribution is divided between $R_{PI,gas}$, related to diffusion within the small pores of MPL and CL, and $R_{PI,ion}$, related to a region close to the Pt surface; (B) Pressure dependent component of the mass transport resistance evaluated at BoT and after 1000 cycles of Combined AST for the three tested CCMs; (C) Local oxygen mass transport resistance, determined as the slope of the relation between mass transport resistance and the inverse of the roughness factor (see Figure SI-8), for the three tested CCMs.

4.3. Realistic automotive ageing prediction

To evaluate and to predict how the performance of PEMFC is altered under practical applications, the MEA energy efficiency and the Pt active surface area are quantified over 2000 cycles of the Combined AST and validated over 1000 operating hours of the single cell DLC protocol. The overall cycle efficiency is reported for CCM B exploiting the abovementioned definition (Equation 3), here evaluated over an entire combined cycle, *i.e.* combining one cycle of low power and one cycle of high power AST. In Figure 8.B the results of this computation are included. The efficiency drops from 56% to 53% in 1000 combined cycles, mirroring the trend recorded during 1000 real drive cycle operating hours, reported in black in the same chart. These results prove that the AST is able to resemble not only the ECSA and the irreversible voltage drops with a 10-fold acceleration factor on the total testing time, as detailed previously, but it is also a useful tool for describing the interrelation

between the irreversible and the reversible ageing phenomena caused by realistic and non-continuous operations. Once being validated over 1000 operating hours, the Combined AST was used to predict the degradation for a longer operational time. Continuing with the protocol up to 2000 cycles, it is quantified an additional decrease of efficiency equal to 1% (from 53% to 52%), against the 3% of the first 1000 cycles. Such a trend proved the progressive stabilization of performance. Consistently, the power peak, which fall as -64 µW cm^{-2} $cycle^{-1}$ in the first 1000 cycles, more than halves its rate of reduction in the additional 1000 cycles (-26 µW cm^{-2} $cycle^{-1}$). By repeating the test up to 2000 cycles, an estimation of the probable evolution of the ECSA parameter over a range of 2000 operating hours, relevant for automotive applications, has been provided too: in the range 1000-2000 cycles, the ECSA varies of just 8%, 4% and 5% for CCM A, B and C respectively (Figure 8.A e Figure SI-9). Probably, the observed electrochemical Ostwald ripening process continues to occur, but at a much slower rate. Figure 8.C shows instead the mass activity based on HFR-free current density at 0.9 V. The mass activity largely dropped at the beginning, within the first 400 cycles, consistently to the ECSA profile. During this initial period, the decrease is about 21% and it finally reaches the 31% at 2000 combined cycles.

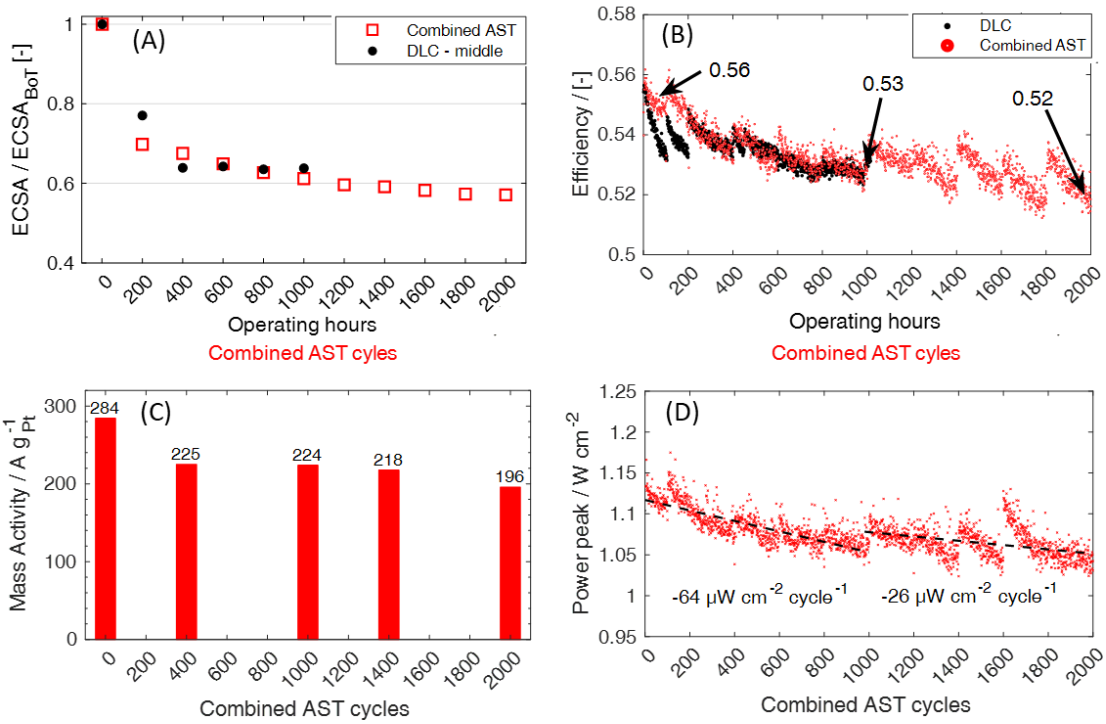

Figure 8 (A) Profile of the ECSA decay measured every 200th combined AST cycles for CCM B; (B) operando efficiency of CCM B evaluated alongside 2000 cycles of Combined AST and compared against 1000 real load cycle (DLC) operating hours; (C) Mass activity computed from the current density at 0.9 V of the oxygen polarization curve and normalized to the initial Pt mass in the cathode catalyst layer. The polarization voltage was corrected for the ohmic resistance and the current density was corrected for H_2 gas crossover; (D) Power peak measured during the operation of the Combined AST (at current "e" of the protocol) and linear fitting over the first 1000 cycles compared against 1000-2000 cycles fitting.

5. Conclusions

This work shows the results of an innovative accelerated protocol for zero-gradient hardware able to mimic the ageing under automotive-like operations. To be claimed as representative, the developed Combined AST is performed in hydrogen/air, and it includes cycling of loads, gas feeding humidification and pressures, as well as it comprises stops procedures, namely short stops and long stops. Load cycling embraces a proper number of potential transitions within a realistic voltage window, that considers state-of-the-art system mitigation strategies.

It was proved that 1000 cycles of the accelerated protocol are able to describe the degradation induced by 1000 operating hours of the realistic driving operation on three different state-of-the-art CCMs. The accelerated protocol introduces a 7-fold acceleration on the operative time basis, resulting in a 10-fold acceleration on the total testing time (*i.e.* including also the stops protocols), being thus advantageous for testing purposes at a laboratory scale. The ageing was validated against: (*i*) ECSA decay, (*ii*) Pt NP size distribution, (*iii*) voltage loss; (*iv*) mass transport limitations, (*v*) efficiency loss. The main degradation is attributed to the cathode catalyst layer. Electrochemical Ostwald ripening mechanism is responsible of catalyst ageing: the large increase in particle size (the average volume/area diameter increased from 4.8 nm to 7.3 nm) is aligned to the ECSA decay, while there were no signs of Pt band formation and carbon support corrosion. The largest variation of Pt active surface area is in the first 100-200 combined cycles. Evolutions are similar for all the materials and reach a value of retained ECSA at 1000 cycles that is 61%-66%. These results significantly differ from what obtained by standard Electrocatalyst AST, characterized by a larger rate of decay in time that drastically reduces the ECSA to non-realistic values. The oxygen mass transport resistance increased with ageing, being thus responsible of the more promoted performance drop at the high load with respect to the low load operation (power decays 3÷6 times more at maximum load than at the minimum). The increase was attributed to the ionomer/catalyst interface contribution that, through a simple estimation, appears more pronounced than in Electrocatalyst AST, while both the molecular and the Knudsen diffusion in pores are mostly unvaried.

Both reversible and irreversible degradation phenomena are mimicked by the new protocol, that was used for longer functioning predictions. AST up to 2000 cycles proved the progressive stabilization of performance. The largest decays of efficiency, mass activity and power are encompassed in the initial part of the protocol. In the range 1000-2000 cycles, just minor changes of ECSA (4÷8%) and efficiency (~1%) are detected. The result highlighted the specific necessity of focusing on the processes that dominate the rate of decay of the Pt active surface area and of performance in the first hundreds of operating hours to improve the technology lifetime.

CRediT authorship contribution statement

Elena Colombo: Methodology, Conceptualization, Investigation, Formal analysis, Data curation, Writing - Original Draft;
Andrea Baricci: Methodology, Conceptualization, Writing - Review & Editing;
Daniele Mora: Investigation;
Laure Guetaz: Investigation, Writing - Review & Editing;
Andrea Casalegno: Supervision, Project administration.

Acknowledgments

This project has received funding from the Fuel Cells and Hydrogen 2 Joint Undertaking under grant agreement No 779565 *ID-FAST*, in the frame of the European Union Horizon 2020 research and innovation program. Funding was received also from the Italian government (Ministero dell'Ambiente e della Sicurezza Energetica), under the program *Progetto Permanent - Bando MITE PNRR Missione 2 Investimento 3.5 A - RSH2A_0O0012*.

References

[1] J. Zhao, X. Li, A review of polymer electrolyte membrane fuel cell durability for vehicular applications: Degradation modes and experimental techniques, Energy Convers. Manag. 199 (2019) 112022. https://doi.org/10.1016/j.enconman.2019.112022.

[2] https://www.fch.europa.eu/soa-and-targets, (2021).

[3] E. Colombo, A. Baricci, A. Bisello, L. Guetaz, A. Casalegno, PEMFC performance decay during real-world automotive operation: Evincing degradation mechanisms and heterogeneity of ageing, J. Power Sources. 553 (2023) 232246. https://doi.org/10.1016/j.jpowsour.2022.232246.

[4] ID-FAST - Investigations on degradation mechanisms and Definition of protocols for PEM Fuel cells Accelerated Stress Testing; Grant agreement no : 779565; Call : H2020-JTI-FCH-2017-1; D4 . 3 – Analysis of coupling between mechanisms and definition of comb, 2021.

[5] Y. Shao-Horn, W.C. Sheng, S. Chen, P.J. Ferreira, E.F. Holby, D. Morgan, Instability of supported platinum nanoparticles in low-temperature fuel cells, Top. Catal. 46 (2007) 285–305. https://doi.org/10.1007/s11244-007-9000-0.

[6] A.P. Soleymani, L. Bonville, C. Wang, S. Schaefer, J. Waldecker, J. Jankovic, Quantifying key parameters to provide better understating of microstructural changes in polymer electrolyte membrane fuel cells during degradation: A startup/shutdown case study, J. Power Sources. 563 (2023) 232807. https://doi.org/10.1016/j.jpowsour.2023.232807.

[7] Y. Qi, Y. Huang, Z. Gao, C.H. Chen, A. Perego, H. Yildirim, M. Odgaard, T. Asset, P. Atanassov, I. V. Zenyuk, Insight into carbon corrosion of different carbon supports for Pt-based electrocatalysts using accelerated stress tests in polymer electrolyte fuel cells, J. Power Sources. 551 (2022) 232209. https://doi.org/10.1016/j.jpowsour.2022.232209.

[8] P.M. Ngo, T. Karimata, T. Saitou, K. Ito, Effect of current density on membrane degradation under the combined chemical and mechanical stress test in the PEMFCs, J. Power Sources. 556 (2023) 232446. https://doi.org/10.1016/j.jpowsour.2022.232446.

[9] T. Morawietz, M. Handl, C. Oldani, P. Gazdzicki, J. Hunger, F. Wilhelm, J. Blake, K.A. Friedrich, R. Hiesgen, High-Resolution Analysis of Ionomer Loss in Catalytic Layers after Operation, J. Electrochem. Soc. 165 (2018) F3139–F3147. https://doi.org/10.1149/2.0151806jes.

[10] X. Yan, Z. Xu, S. Yuan, A. Han, Y. Shen, X. Cheng, Y. Liang, S. Shen, J. Zhang, Structural and transport properties of ultrathin perfluorosulfonic acid ionomer film in proton exchange membrane fuel cell catalyst layer: A review, J. Power Sources. 536 (2022) 231523. https://doi.org/10.1016/j.jpowsour.2022.231523.

[11] E. Pahon, D. Hissel, N. Yousfi-Steiner, A review of accelerated stress tests dedicated to proton exchange membrane fuel cells – Part I: Fuel cell component level, J. Power Sources. 546 (2022) 231895. https://doi.org/10.1016/j.jpowsour.2022.231895.

[12] S. Stariha, N. Macauley, B.T. Sneed, D. Langlois, K.L. More, R. Mukundan, R.L. Borup, N. Materials, O. Ridge, Recent Advances in Catalyst Accelerated Stress Tests for Polymer Electrolyte Membrane Fuel Cells, J. Electrochem. Soc. 165 (2018) 492–501. https://doi.org/10.1149/2.0881807jes.

[13] EERE, Multiyear Research, Development and Demonstration Plan, Fuel Cells Section, (2016) 1–58. https://doi.org/doi:10.2172/1219578.

[14] Y.-H. Lai, K.M. Rahmoeller, J.H. Hurst, R.S. Kukreja, M. Atwan, A.J. Maslyn, C.S. Gittleman, Accelerated Stress Testing of Fuel Cell Membranes Subjected to Combined Mechanical/Chemical Stressors and Cerium Migration, J. Electrochem. Soc. 165 (2018) F3217–F3229. https://doi.org/10.1149/2.0241806jes.

[15] R.L. Borup, A. Kusoglu, K.C. Neyerlin, R. Mukundan, R.K. Ahluwalia, D.A. Cullen, K.L. More, A.Z. Weber, D.J. Myers, Recent developments in catalyst-related PEM fuel cell durability, Curr. Opin. Electrochem. 21 (2020) 192–200. https://doi.org/10.1016/j.coelec.2020.02.007.

[16] Z. Hua, Z. Zheng, E. Pahon, M.C. Péra, F. Gao, A review on lifetime prediction of proton exchange membrane fuel cells system, J. Power Sources. 529 (2022).

https://doi.org/10.1016/j.jpowsour.2022.231256.

[17] T. Takahashi, T. Ikeda, K. Murata, O. Hotaka, Shigeki Hasegawa, Y. Tachikawa, M. Nishihara, J. Matsuda, T. Kitahara, S.M. Lyth, A. Hayashi, K. Sasaki, Accelerated Durability Testing of Fuel Cell Stacks for Commercial Automotive Applications: A Case Study, J. Electrochem. Soc. 169 (2022) 044523. https://doi.org/10.1149/1945-7111/ac662d.

[18] E. Colombo, A. Bisello, A. Casalegno, A. Baricci, Mitigating PEMFC Degradation During Start-Up: Locally Resolved Experimental Analysis and Transient Physical Modelling, J. Electrochem. Soc. 168 (2021) 054508. https://doi.org/10.1149/1945-7111/abf4eb.

[19] F. Jia, L. Guo, H. Liu, Mitigation strategies for hydrogen starvation under dynamic loading in proton exchange membrane fuel cells, Energy Convers. Manag. 139 (2017) 175–181. https://doi.org/10.1016/j.enconman.2017.02.051.

[20] M. Koprek, R. Schlumberger, C. Wachtel, F. Wilhelm, M. Messerschmidt, J. Scholta, M. Hölzle, Local ageing effects of polymer electrolyte fuel cell membrane electrode assemblies due to accelerated durability testing, Fuel Cells. 22 (2022) 271–283. https://doi.org/10.1002/fuce.202200064.

[21] A. Bisello, E. Colombo, A. Baricci, C. Rabissi, L. Guetaz, P. Gazdzicki, A. Casalegno, Mitigated Start-Up of PEMFC in Real Automotive Conditions: Local Experimental Investigation and Development of a New Accelerated Stress Test Protocol, J. Electrochem. Soc. 168 (2021) 054501. https://doi.org/10.1149/1945-7111/abf77b.

[22] E. Colombo, D. Casadei, A. Baricci, A. Casalegno, An open-source zero-gradient cell hardware to improve and accelerate durability testing of PEM Fuel Cell, under review, HardwareX. (2023).

[23] P.J. Ferreira, G.J. la O', Y. Shao-Horn, D. Morgan, R. Makharia, S. Kocha, H.A. Gasteiger, Instability of Pt/C Electrocatalysts in Proton Exchange Membrane Fuel Cells, J. Electrochem. Soc. 152 (2005) A2256. https://doi.org/10.1149/1.2050347.

[24] D.R. Baker, D.A. Caulk, K.C. Neyerlin, M.W. Murphy, Measurement of Oxygen Transport Resistance in PEM Fuel Cells by Limiting Current Methods, J. Electrochem. Soc. 156 (2009) B991. https://doi.org/10.1149/1.3152226.

[25] T. Bednarek, G. Tsotridis, Assessment of the electrochemical characteristics of a Polymer Electrolyte Membrane in a reference single fuel cell testing hardware, J. Power Sources. 473 (2020) 228319. https://doi.org/10.1016/j.jpowsour.2020.228319.

[26] R. Riasse, C. Lafforgue, F. Vandenberghe, F. Micoud, A. Morin, M. Arenz, J. Durst, M. Chatenet, Benchmarking proton exchange membrane fuel cell cathode catalyst at high current density: A comparison between the rotating disk electrode, the gas diffusion electrode and

differential cell, J. Power Sources. 556 (2023). https://doi.org/10.1016/j.jpowsour.2022.232491.

[27] R.L. Borup, J.R. Davey, F.H. Garzon, D.L. Wood, M.A. Inbody, PEM fuel cell electrocatalyst durability measurements, J. Power Sources. 163 (2006) 76–81. https://doi.org/10.1016/j.jpowsour.2006.03.009.

[28] T. Jahnke, A. Baricci, C. Rabissi, A. Casalegno, Physical Modeling of Catalyst Degradation in Low Temperature Fuel Cells: Platinum Oxidation, Dissolution, Particle Growth and Platinum Band Formation [J. Electrochem. Soc. , 167 , 013523 (2020)], J. Electrochem. Soc. 167 (2020) 149001. https://doi.org/10.1149/1945-7111/abbfda.

[29] P. Zihrul, I. Hartung, S. Kirsch, G. Huebner, H.A. Gasteiger, Voltage Cycling Induced Losses in Electrochemically Active Surface Area and in H 2 / Air-Performance of PEM Fuel Cells, 163 (2016) 492–498. https://doi.org/10.1149/2.0561606jes.

[30] A. Kneer, N. Wagner, C. Sadeler, A. Scherzer, D. Gerteisen, Effect of Dwell Time and Scan Rate during Voltage Cycling on Catalyst Degradation in PEM Fuel Cells, 165 (2018) 805–812. https://doi.org/10.1149/2.0651810jes.

[31] H. Yu, A. Baricci, A. Bisello, A. Casalegno, L. Guetaz, L. Bonville, R. Maric, Strategies to mitigate Pt dissolution in low Pt loading proton exchange membrane fuel cell: I. A gradient Pt particle size design, Electrochim. Acta. 247 (2017) 1155–1168. https://doi.org/10.1016/j.electacta.2017.07.093.

[32] L. Hu, T. Van Cleve, H. Yu, J. Hyung, N. Kariuki, A.J. Kropf, R. Mukundan, D.A. Cullen, D.J. Myers, C. Neyerlin, Electrochemical characterization of evolving ionomer / electrocatalyst interactions throughout accelerated stress tests, J. Power Sources. 556 (2023) 232490. https://doi.org/10.1016/j.jpowsour.2022.232490.

[33] A. Baricci, M. Bonanomi, H. Yu, L. Guetaz, R. Maric, A. Casalegno, Modelling analysis of low platinum polymer fuel cell degradation under voltage cycling: Gradient catalyst layers with improved durability, J. Power Sources. 405 (2018) 89–100. https://doi.org/10.1016/j.jpowsour.2018.09.092.

[34] A. Kongkanand, M.F. Mathias, The Priority and Challenge of High-Power Performance of Low-Platinum Proton-Exchange Membrane Fuel Cells, J. Phys. Chem. Lett. 7 (2016) 1127–1137. https://doi.org/10.1021/acs.jpclett.6b00216.

[35] A. Grimaldi, A. Baricci, S. De Antonellis, C. Oldani, A. Casalegno, Experimental study and modeling of water transport through short-side-chain perfluorosulfonic acid membranes, J. Power Sources. 558 (2023) 232556. https://doi.org/10.1016/j.jpowsour.2022.232556.

[36] P. Gazdzick, J. Mitzel, D. Sanchez, M. Schulze, K.A. Friedrich, Evaluation of reversible and

irreversible degradation rates of polymer electrolyte membrane fuel cells tested in automotive conditions, J. Power Sources. 327 (2016) 86–95. https://doi.org/10.1016/j.jpowsour.2016.07.049.

[37] J. Mitzel, Q. Zhang, P. Gazdzicki, K.A. Friedrich, Review on mechanisms and recovery procedures for reversible performance losses in polymer electrolyte membrane fuel cells, J. Power Sources. 488 (2021) 229375. https://doi.org/10.1016/j.jpowsour.2020.229375.

[38] B. Li, K. Wan, M. Xie, T. Chu, X. Wang, X. Li, D. Yang, P. Ming, C. Zhang, Durability degradation mechanism and consistency analysis for proton exchange membrane fuel cell stack, Appl. Energy. 314 (2022) 119020. https://doi.org/10.1016/j.apenergy.2022.119020.

[39] R.K.F. Della Bella, B.M. Stühmeier, H. Gasteiger, Universal Correlation between Cathode Roughness Factor and H 2 /Air Performance Losses in Voltage Cycling-Based Accelerated Stress Tests , J. Electrochem. Soc. (2022). https://doi.org/10.1149/1945-7111/ac67b8.

[40] K. Shinozaki, S. Kajiya, S. Yamakawa, N. Hasegawa, T. Suzuki, M. Shibata, R. Jinnouchi, Investigation of gas transport resistance in fuel cell catalyst layers via hydrogen limiting current measurements of CO-covered catalyst surfaces, J. Power Sources. 565 (2023) 232909. https://doi.org/10.1016/j.jpowsour.2023.232909.

[41] N. Nonoyama, S. Okazaki, A.Z. Weber, Y. Ikogi, T. Yoshida, Analysis of Oxygen-Transport Diffusion Resistance in Proton-Exchange-Membrane Fuel Cells, J. Electrochem. Soc. 158 (2011) B416. https://doi.org/10.1149/1.3546038.

[42] T.A. Greszler, D. Caulk, P. Sinha, The Impact of Platinum Loading on Oxygen Transport Resistance, J. Electrochem. Soc. 159 (2012) F831–F840. https://doi.org/10.1149/2.061212jes.

[43] V. Yarlagadda, N. Ramaswamy, R.S. Kukreja, S. Kumaraguru, Ordered mesoporous carbon supported fuel cell cathode catalyst for improved oxygen transport, J. Power Sources. 532 (2022) 231349. https://doi.org/10.1016/j.jpowsour.2022.231349.

[44] F. Du, T.A. Dao, P.V.J. Peitl, A. Bauer, K. Preuss, A.M. Bonastre, J. Sharman, G. Spikes, M. Perchthaler, T.J. Schmidt, A. Orfanidi, Effects of PEMFC Operational History under Dry/Wet Conditions on Additional Voltage Losses due to Ionomer Migration, J. Electrochem. Soc. 167 (2020) 144513. https://doi.org/10.1149/1945-7111/abc83f.

[45] J.P. Owejan, J.E. Owejan, W. Gu, Impact of Platinum Loading and Catalyst Layer Structure on PEMFC Performance, J. Electrochem. Soc. 160 (2013) F824–F833. https://doi.org/10.1149/2.072308jes.